ACS ES&T Engineering

pubs.acs.org/estengg

Article

Regulation on the Exposure Degree and Lewis Acidity of Fe−O Sites in Fe-MOGs for Photocatalytic Oxidation of *o*-Xylene

Published as part of ACS ES&T Engineering special issue "Environmental Catalysis for Air Pollution Control."

Lu Chen, Guanqing Song, Xiao Wang,* Chi Song, Haijiao Xie, Jing Sun,* Fan Dong, and Deliang Chen*

Cite This: https://doi.org/10.1021/acsestengg.4c00949

Read Online

ABSTRACT: Adsorption and catalytic sites in photocatalysts are important factors influencing the degradation efficiency of aromatic volatile organic compounds (VOCs), and their accurate regulation is the prerequisite to reveal the photocatalytic oxidation (PCO) mechanisms. Herein, by adjusting the molar ratio between Fe salts and H_3BTC linkers, the coordinate saturation degree and Lewis acidity of open Fe−O sites in Fe-MOGs were successfully modulated, which follows the order of $Fe_1BTC_{0.5}$ > Fe_1BTC_1 > Fe_1BTC_2. The highly exposed Fe−O sites ($Fe_1BTC_{0.5}$) not only promote the adsorption of *o*-xylene via Lewis acid−base and $\pi-\pi$ interactions but also accelerate the generation of oxidative ·OH and $\cdot O_2^-$ radicals by providing active open metal sites (OMSs). However, highly exposed Fe−O sites inhibit the release of benzyl midproducts, which detriments the performance of $Fe_1BTC_{0.5}$. Fe_1BTC_1 with an appropriate exposure degree of Fe−O sites and excellent photoelectric properties shows moderate affinity to *o*-xylene and sufficient oxidative radicals, which enable the efficient and stable removal of *o*-xylene (80% for at least 180 min). *In situ* diffuse reflection infrared Fourier transform (DRIFT) spectra reveal the impacts of exposure degree of Fe−O sites on the PCO pathway of *o*-xylene. Our study provides novel insights into the role of adsorption and catalytic sites in the elimination of aromatic VOCs.

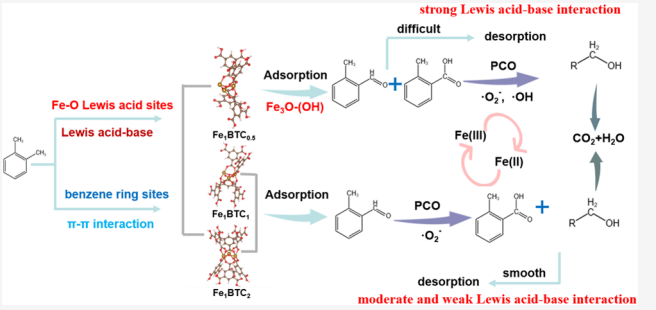

KEYWORDS: *exposure degree of Fe−O sites, Lewis acid−base interaction, $\pi-\pi$ interaction, PCO, o-xylene*

1. INTRODUCTION

The trend of air quality deterioration in China has been somewhat curbed since the implementation of the Action Plan for Air Pollution Prevention and Control over the past ten years. However, the existing environmental issues are still not optimistic. Volatile organic compounds (VOCs), especially aromatic VOCs emitted from decoration materials and furniture in interior space, may seriously harm the nervous and endocrine systems of the human body.[1−3] Semiconductor photocatalytic oxidation (PCO) is an effective means to remove aromatic VOCs by utilizing reactive oxygen species generated by the excited electrons and holes under light irradiation.[4−6]

Semiconductor PCO of aromatic VOCs is a typical heterogeneous gas−solid reaction. The adsorption and catalytic sites of photocatalysts determine not only the oxidation efficiency but also the degradation routes of VOCs. Metal−organic gels (MOGs) as semiconductor-like materials are a kind of monolithic metal−organic frameworks (MOFs), in which central metal atoms coordinate with organic ligands to form tertiary building units and further assemble into 3D frameworks through weak hydrogen bonds, $\pi-\pi$ stacking, and van der Waals forces.[7−10] Benefiting from the hierarchical porous structure and the exposure of active sites, MOGs have attracted widespread attention in adsorption, sensing, separation, catalysis, and pharmaceuticals.[11−15] The open metal sites (OMSs) as Lewis acid sites in MOGs are beneficial for trapping and adsorbing aromatic VOCs by Lewis acid−base interaction. Combining with an internal photogenerated charge transfer mechanism, they display a significant advantage in PCO of aromatic VOCs.[16,17] Hupp et al. treated UiO-67(Zr) with hydrochloric acid (HCl) to enable the partial exposure of Zr−O catalytic active sites. Compared with pristine UiO-67(Zr), which exhibited almost no PCO activity toward styrene, UiO-67(Zr) after treatment showed a degradation efficiency of 40% toward styrene,[18] indicating that the exposure of catalytic active sites was essential for PCO of aromatic

Received: December 23, 2024
Revised: February 25, 2025
Accepted: March 7, 2025

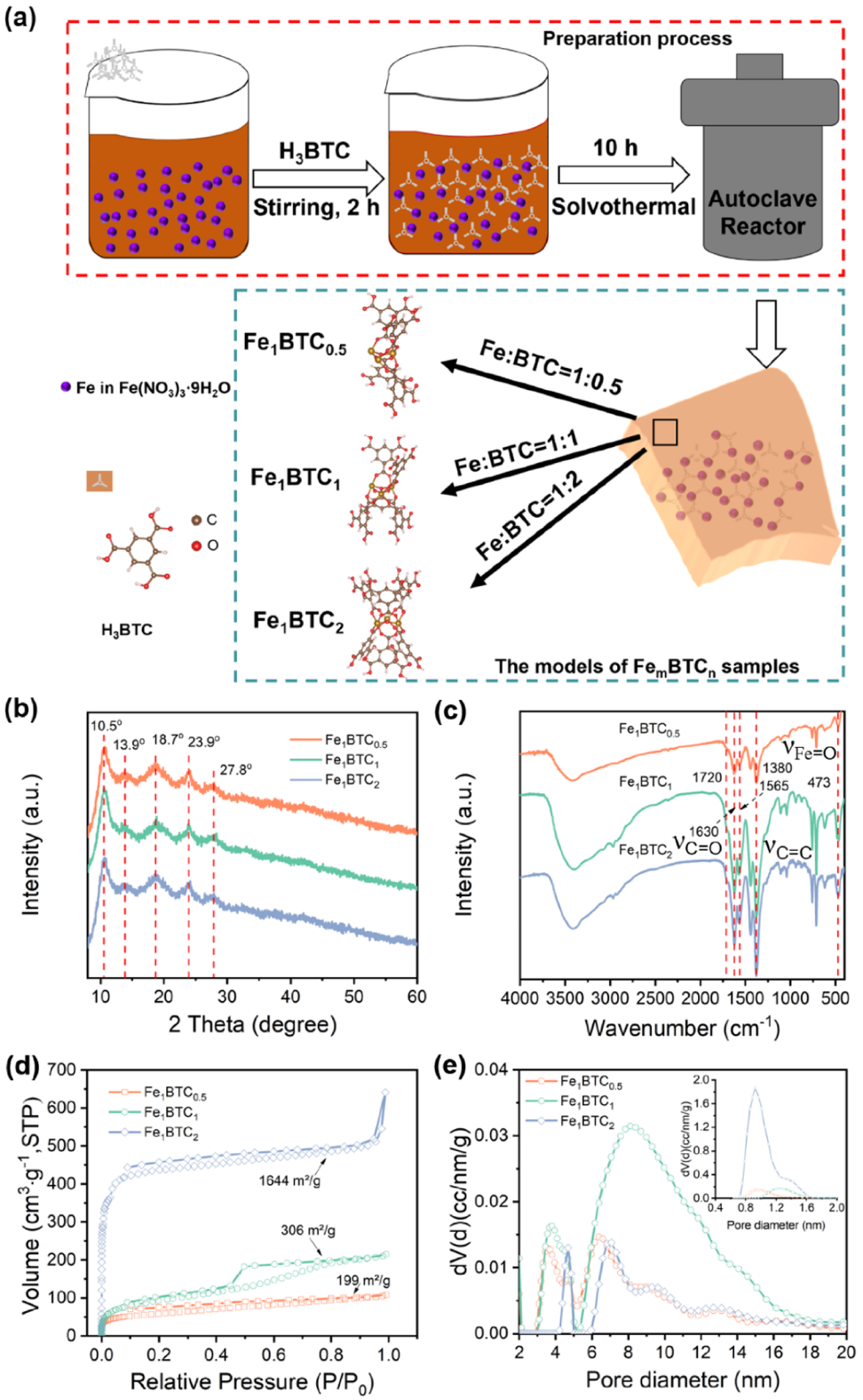

Figure 1. (a) Diagram for the synthesis of Fe_mBTC_n samples. (b) XRD patterns, (c) FTIR spectra, (d) N_2 adsorption−desorption isotherms, and (e) pore-size distribution curves of Fe_mBTC_n.

VOCs. Park et al. prepared a series of Ti-MOFs by adjusting the molar ratios of two organic linkers (H_2BDC and NH_2−H_2BDC), which not only provided more adsorption sites for toluene but also endowed good charge separation ability to improve photocatalytic performance.[19] Sun et al. prepared a series of carbon quantum dots (CQDs) modified UiO-66 MOG composites (CQD/UiO-66 MOG). Benefiting from the adsorption sites provided by UiO-66 MOG and CQDs, the composites showed a high toluene adsorption capacity (29.06 μmol/g) and PCO efficiency.[20] Therefore, adsorption and catalytic sites of photocatalysts show an important impact on the efficiency of oxidation of aromatic VOCs. However, the

https://doi.org/10.1021/acsestengg.4c00949
ACS EST Engg. XXXX, XXX, XXX−XXX

roles of adsorption and catalytic sites in determining the PCO paths of aromatic VOCs have not been discussed in detail.

The accurate control of the type and distribution of adsorption and catalytic sites is the key to clarify their roles in PCO of aromatic VOCs. Adjusting the exposure degree of metal clusters in MOGs, which can act as both adsorption and catalytic active sites, offers an effective means.[21] Among a variety of MOGs, Fe-MOGs exhibited great potential in PCO of aromatic VOCs due to the strong affinity of Fe−O clusters for aromatic VOCs.[22,23] Previously, Fe-MOF/MOG homojunction composites were prepared. It was identified that the exposed Fe−O clusters played a crucial role in capturing and PCO of aromatic VOCs.[22] Furthermore, Ag@Fe-MOG composites featuring a novel "watermelon-seed" structure were developed via a facile quasi-in situ synthesis approach, which demonstrated that the exposed Fe−O clusters and metal Ag clusters synergistically promoted PCO of *o*-xylene.[24] However, the influence of the exposure degree of Fe−O clusters in the adsorption and PCO processes of aromatic VOCs in Fe-MOGs remains inadequately investigated. Benefiting from the high coordination activity of Fe(III), the defect tolerance of Fe−O coordination during the preparation of Fe-MOGs can be easily improved by regulating the dynamic equilibrium of crystal nucleation and growth.[25−27] Mahmood et al.[28] synthesized FeAl-MOGs by varying the quantities of Fe and Al precursors, capitalizing on the differences of coordination between metal central atoms Fe and Al with organic ligands. This approach facilitated heterogeneous mismatched growth, resulting in the differential exposure of metal oxide clusters and achieving rapid and high-capacity adsorption of methyl orange and rhodamine B at low pH. Previously, we harnessed the differences in electron affinity between Fe(III) and Na(I) to modulate the coordination and Lewis acidity of Fe−O clusters in Fe-MOGs, thereby enabling the selective capture and PCO of electron-rich *o*-xylene and electron-deficient acetaldehyde.[23] Therefore, the exposure degree of Fe−O sites in Fe-MOGs is easy to regulate to adjust their adsorption (Fe−O clusters and organic ligands) and catalytic (Fe−O clusters) sites with interacting aromatic VOCs.

In this work, the exposure degree and Lewis acidity of Fe−O sites in Fe-MOGs were regulated by adjusting the additive amounts of Fe-source and organic ligand. The exposure degree of Fe−O sites was characterized by XPS, TPD, and contact angle experiments. *O*-xylene, a quintessential aromatic VOC, was selected as the target pollutant. It constitutes a notable byproduct in the coating industry and is among the principal atmospheric contaminants in urban air, presenting significant health hazards to humans.[29,30] The Lewis acid−base interaction between the exposed Fe−O sites and *o*-xylene and $\pi-\pi$ interaction between ligands and *o*-xylene were studied by density functional theory (DFT) calculation and adsorption experiments. The relation between the exposure degree of Fe−O sites and the photoelectric properties of the samples was discussed, unveiling their influences on the PCO performance of *o*-xylene. The roles of Fe−O sites with different exposure degrees in Fe-MOGs during the adsorption and PCO of *o*-xylene were further analyzed by *in situ* diffuse reflection infrared Fourier transform (DRIFT) spectra and the mechanism of PCO of *o*-xylene was suggested.

2. EXPERIMENTAL SECTION

2.1. Preparation of Samples. Fe-MOGs (MIL-100(Fe) MOGs) with different exposure degrees and Lewis acidity of Fe−O sites were prepared by regulating the ratio between Fe-source and organic ligand using the solvothermal method. These MIL-100(Fe) MOGs are labeled as Fe_mBTC_n, where *m* and *n* represent the molar dosage of $Fe(NO_3)_3{\cdot}9H_2O$ and 1,3,5-benzenetricarboxylic acid (H_3BTC) used in the synthesis, respectively. $Fe_1BTC_{0.5}$, Fe_1BTC_1, and Fe_1BTC_2 were finally acquired. The detailed process of sample preparation is presented in the Supporting Information (SI) Text S2.

2.2. Materials Characterization. The physicochemical properties of Fe_mBTC_n were characterized by X-ray diffraction (XRD), Fourier transform infrared (FTIR) spectroscopy, field emission scanning electron microscopy (SEM), transmission electron microscopy (TEM), X-ray photoelectron spectroscopy (XPS), temperature-programmed desorption (TPD), contact angle, thermogravimetric analysis (TGA), UV−vis diffuse reflectance spectra (UV−vis), fluorescence spectrum (PL), electron paramagnetic resonance spectroscopy (EPR), *in situ* diffuse reflection infrared Fourier transform (DRIFT) spectra, and density functional theory (DFT) for first principle calculations. The relevant characterization details are described in SI Text S3.

2.3. Performance Evaluation of Fe_mBTC_n. The adsorption and PCO of *o*-xylene on Fe_mBTC_n were performed on a self-built reaction system (Figure S1) reported in our previous work.[22,23] The adsorption and PCO performance of Fe_mBTC_n were tested at room temperature with a relative humidity of 60% to simulate the atmospheric environment. The detailed experimental conditions for evaluating the adsorption and PCO performance of Fe_mBTC_n are shown in SI Text S5.

3. RESULTS AND DISCUSSION

3.1. Compositions, Porous Characteristics, and Morphologies of Fe_mBTC_n. The preparation route of Fe_mBTC_n is schematically shown in Figure 1a. $Fe(NO_3)_3{\cdot}9H_2O$ and H_3BTC act as the iron source and organic ligand, respectively. A series of Fe-MOGs were obtained by adjusting the dosage of organic ligands. The phase composition of Fe_mBTC_n was analyzed by XRD. In Figure 1b, the characteristic peaks appear in the 2θ range from 5 to 30° corresponding to MIL-100(Fe) (Figure S2), and the diffraction at 2θ from 30 to 60° is not observed in Fe_mBTC_n, confirming that oxidized Fe is not generated during synthesis.[31,32] Besides, in Figure 1c of FTIR spectra, the bands at 1565−1380 and 1630 cm^{-1} corresponding to the characteristic peaks of the benzene ring and the stretching vibration of C = O in H_3BTC are found. The band at 480 cm^{-1} is assigned to the stretching vibration of Fe−O formed by the coordination of carboxyl oxygen in H_3BTC and Fe(III).[31] Notably, the band intensity of the stretching vibration of uncoordinated C = O in H_3BTC at 1720 cm^{-1} increases with the addition of H_3BTC, indicating the presence of more uncoordinated carboxyl groups. As shown in Figure 1d and e, N_2 adsorption−desorption isotherms and pore-size distribution curves of Fe_mBTC_n are drawn according to the model of nonlocal density functional theory (NLDFT). In Figure 1d, the NLDFT cumulative surface areas of $Fe_1BTC_{0.5}$, Fe_1BTC_1, and Fe_1BTC_2 are 199, 306, and 1644 $m^2\,g^{-1}$, respectively, confirming that the cumulative surface area of Fe_mBTC_n gradually increases with

https://doi.org/10.1021/acsestengg.4c00949
ACS EST Engg. XXXX, XXX, XXX−XXX

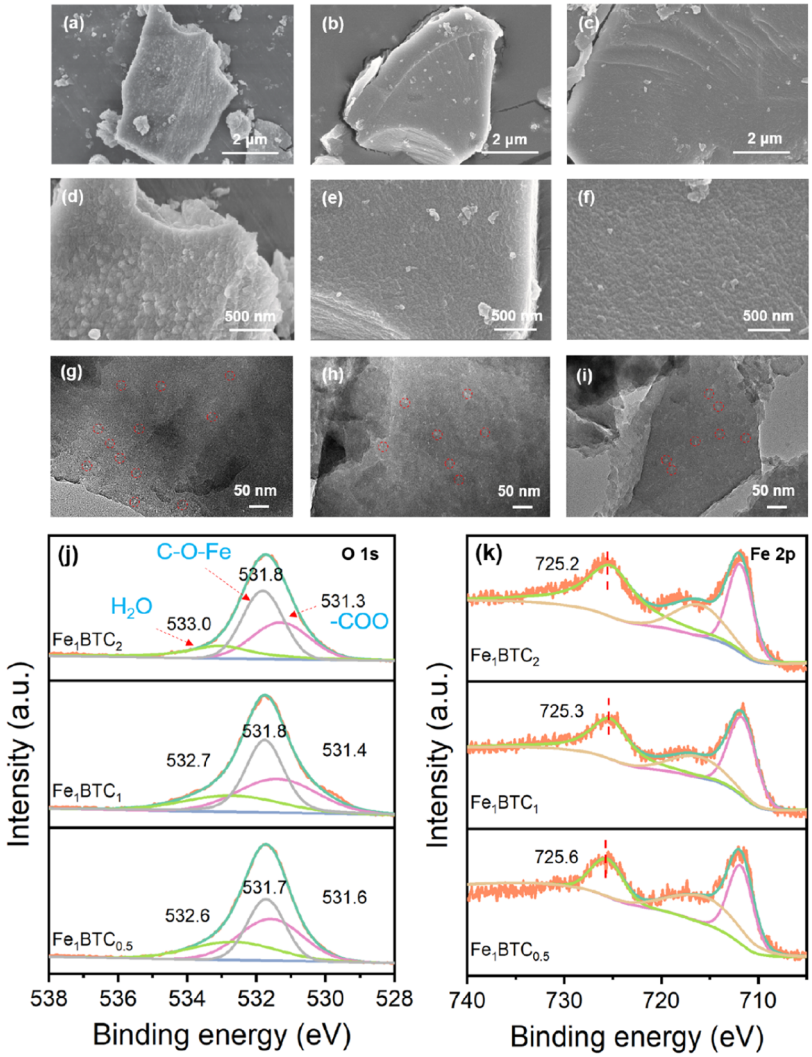

Figure 2. (a–f) SEM images of (a, d) $Fe_1BTC_{0.5}$, (b, e) Fe_1BTC_1, and (c, f) Fe_1BTC_2. (g–i) TEM images of Fe_1BTC_1. (j, k) The XPS spectra of O 1s (j) and Fe 2p (k) in Fe_mBTC_n.

the dosage of H_3BTC. $Fe_1BTC_{0.5}$, Fe_1BTC_1, and Fe_1BTC_2 display type-II, IV, and I N_2 isotherm curves in the low P/P_0 region, respectively, which indicates the existence of abundant micropores in all of the Fe_mBTC_n samples. Unlike the H1-type hysteresis adsorption isotherms of $Fe_1BTC_{0.5}$ and Fe_1BTC_2, H2-type hysteresis adsorption isotherm is observed in Fe_1BTC_1, reflecting that the pore-size distribution is relatively uniform. In Figure 1e, the pore-size distribution of Fe_mBTC_n is further discussed. In all samples, mesopores with pore sizes over 2 nm are found, and Fe_1BTC_1 exhibits the most amount of mesoporous among the samples, which is beneficial to the free migration of *o*-xylene molecules in the pores.[33,34] Compared with $Fe_1BTC_{0.5}$ and Fe_1BTC_1, Fe_1BTC_2 presents the highest concentration of micropores with pore sizes of less than 2 nm, corresponding to its high specific surface area (1644 $m^2\ g^{-1}$). Based on the above results, the hypothesis can be inferred that the long-range ordering of the MIL-100(Fe) crystals is disrupted, and highly exposed Fe–O sites are formed when H_3BTC is short during the synthesis of Fe_mBTC_n, resulting in smaller NLDFT cumulative surface area. With the increase of H_3BTC dosage, the central metal atom Fe inclines to coordinate saturation with oxygen atoms in the carboxylic acid groups, leading to a low exposure degree of Fe–O sites with high NLDFT cumulative surface area.

To further confirm this assumption, the micromorphology of the samples was studied by SEM. In Figures 2a–f and S3a–f, $Fe_1BTC_{0.5}$, Fe_1BTC_1, and Fe_1BTC_2 all exhibit bulk morphology, matched well with MIL-100(Fe) MOG reported previously.[35] As shown in Figure 2a,d, small protrusions on the surface of $Fe_1BTC_{0.5}$ are obviously observed. However, Fe_1BTC_1 and Fe_1BTC_2 display a flat surface in Figure 2b,e and c,f, which is attributed to the coordination of Fe–O clusters with BTC^{3-} links. Fe, C, and O elements are uniformly distributed in Fe_1BTC_1, confirmed by the EDS results in Figure S3g. According to the TEM images in Figure 2g–i, a large number of channels are observed in Fe_1BTC_1, consistent with the porous network structure of gel materials.

XPS was applied to deeply research the coordination of Fe atoms and electronic state of elements in Fe_mBTC_n. Fe, C, and O are observed in Fe_mBTC_n (Figure S4), consistent with area scan results of EDS. In Figure 2j, O 1s is divided into three peaks through deconvolution fitting. And the peaks at 531.6 and 531.7 eV in $Fe_1BTC_{0.5}$ correspond to carboxyl groups (–COO) and the tertiary building units (TBU, C–O–Fe), respectively.[36] Besides, the weak shoulder peak at 532.6 eV is

https://doi.org/10.1021/acsestengg.4c00949
ACS EST Engg. XXXX, XXX, XXX–XXX

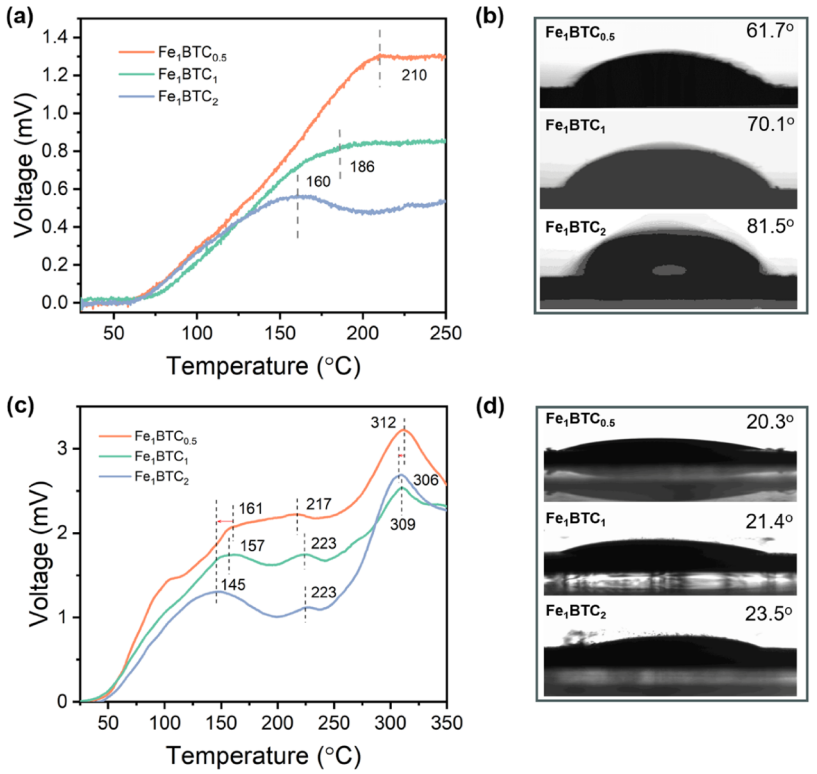

Figure 3. (a) Temperature-programmed desorption (TPD)-NH_3 curves of Fe_mBTC_n. (b) Contact angles of H_2O on Fe_mBTC_n. (c) TPD-*o*-xylene curves of Fe_mBTC_n. (d) Contact angles of *o*-xylene on Fe_mBTC_n.

classified as H_2O adsorbed on the surface of $Fe_1BTC_{0.5}$.[36] Compared with $Fe_1BTC_{0.5}$ (531.7 eV for C−O−Fe), a slight blue shift of 0.1 eV in the binding energy of O 1s for Fe_1BTC_1 and Fe_1BTC_2 (531.8 eV for C−O−Fe) happens, respectively, suggesting the decrease in the electron density of O species due to the coordination of more carboxyl groups in H_3BTC with Fe. The opposite results are observed that the −COO of O 1s in Fe_1BTC_1 (531.4 eV) and Fe_1BTC_2 (531.3 eV) shift to lower binding energy compared with $Fe_1BTC_{0.5}$ (531.6 eV) due to leaving more uncoordinated −COO with the addition of high concentration of H_3BTC. While the peak (532.6 eV) assigned to H_2O adsorbed on the surface of $Fe_1BTC_{0.5}$ shifts to 532.7 eV in Fe_1BTC_1 and 533.0 eV in Fe_1BTC_2 as a result of the reduced exposure degree of Fe−O clusters. As shown in Table S1, the proportions of the three peaks are calculated by fitting the peak areas. Compared with $Fe_1BTC_{0.5}$ (40.5%), the proportion of −COO gradually decreases (Fe_1BTC_1 ∼ 37.0% and Fe_1BTC_2 ∼ 34.5%), while the proportion of C−O−Fe ($Fe_1BTC_{0.5}$ ∼ 35.5%) increases to 41.9% in Fe_1BTC_1 and 45.8% in Fe_1BTC_2. This is because the exposed Fe−O clusters reacted with the added H_3BTC to achieve saturation coordination for building a complete framework of Fe_mBTC_n. Besides, the proportion of H_2O adsorbed on the surface in $Fe_1BTC_{0.5}$ reaches 24%, which declines to 21.1 and 19.7% in Fe_1BTC_1 and Fe_1BTC_2, respectively, mainly due to the decrease in exposure degree of Fe−O Lewis acid sites, which agreed well with the changes in the proportion of −COO and C−O−Fe peaks. In Figure 2k, the peak of Fe $2p_{1/2}$ at 725.6 eV corresponding to Fe(III) is observed in $Fe_1BTC_{0.5}$. A red shift happens in Fe_1BTC_1 (725.3 eV) and Fe_1BTC_2 (725.2 eV), indicating an increase in the electron density of Fe species, which further demonstrates the higher coordination saturation degree of Fe in Fe_1BTC_1 and Fe_1BTC_2 than in $Fe_1BTC_{0.5}$.[37] The XPS results provide the direct evidence that the Fe−O clusters gradually approach coordination saturation with the addition of BTC^{3-} linkers, resulting in a decrease in the exposure degree of Fe−O clusters ($Fe_1BTC_{0.5}$ > Fe_1BTC_1 > Fe_1BTC_2). Therefore, the hypothesis that the exposure degree of Fe−O clusters in Fe_mBTC_n has been successfully regulated by adjusting the dosage of H_3BTC is proved.

3.2. Characterization of the Exposure Degree and Lewis Acidity of Fe−O Sites in Fe_mBTC_n. The exposure degree of Fe−O sites showing Lewis acidity in Fe_mBTC_n was characterized by NH_3-TPD. A classification ordination for acid sites was proposed by Topsøe et al. assigning the peaks below 200 °C and between 200 and 400 °C to probe molecules desorbed from weak and medium strong acid sites.[38] As shown in Figure 3a, $Fe_1BTC_{0.5}$ shows a significant desorption peak at 210 °C, which belongs to medium Lewis acid sites. The peak gradually shifts toward the low-temperature direction to 186 °C (Fe_1BTC_1) and 160 °C (Fe_1BTC_2), which is defined as weak Lewis acid sites. Furthermore, the intensities of the desorption peaks gradually decrease from $Fe_1BTC_{0.5}$ to Fe_1BTC_2, indicating that the strength of Lewis acidity of Fe−O sites is the highest in $Fe_1BTC_{0.5}$, and it is gradually reduced with the addition of H_3BTC. Owing to the positive correlation between Lewis acidity and exposure degree of Fe−O sites in Fe_mBTC_n, the exposure degree of Fe−O sites also gradually decreases from $Fe_1BTC_{0.5}$ to Fe_1BTC_2 ($Fe_1BTC_{0.5}$ > Fe_1BTC_1 > Fe_1BTC_2). To further confirm this result, the affinity between the surface interface of Fe_mBTC_n and water molecules, another representative alkaline probe molecules, was tested through contact angle experiments.[39] In Figure 3b, the contact angles of the samples are all less than 90°, while they gradually increased from 61.7° of $Fe_1BTC_{0.5}$ to 70.1° of $Fe_1BTC_{0.5}$ and 81.5° of Fe_1BTC_2, which proves that the affinity

https://doi.org/10.1021/acsestengg.4c00949
ACS EST Engg. XXXX, XXX, XXX−XXX

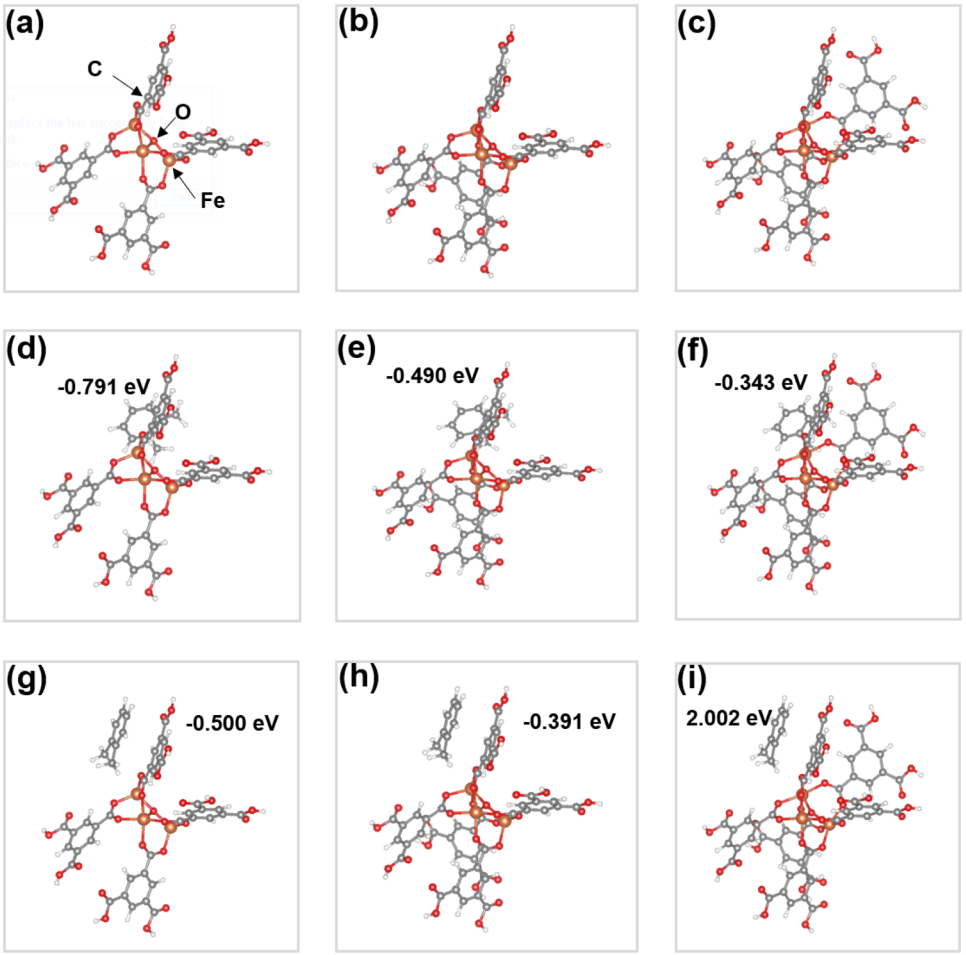

Figure 4. (a–c) Stable structures by optimizing poscar catalyst clusters: $Fe_1BTC_{0.5}$ (a), Fe_1BTC_1 (b), and Fe_1BTC_2 (c). (d–f) The adsorption energies (ΔE) of *o*-xylene on the Fe–O Lewis acid sites in $Fe_1BTC_{0.5}$ (d), Fe_1BTC_1 (e), and Fe_1BTC_2 (f). (g–i) The adsorption energies (ΔE) of *o*-xylene on the benzene ring sites in $Fe_1BTC_{0.5}$ (g), Fe_1BTC_1 (h), and Fe_1BTC_2 (i).

between the exposed Fe–O Lewis acid sites in Fe_mBTC_n and water molecules is strong and gradually weakens with the addition of H_3BTC, reflecting a decrease in the exposure degree of Fe–O Lewis acid sites from $Fe_1BTC_{0.5}$ to Fe_1BTC_1 and Fe_1BTC_2. The conclusion can be drawn that the exposure degree and Lewis acidity of Fe–O sites in Fe_mBTC_n were successfully adjusted by controlling the dosage of H_3BTC.

TPD was also carried out to reveal the adsorption behavior of *o*-xylene on Fe_mBTC_n. Prior to TPD analysis, thermogravimetric experiments were conducted and the results displayed that the structures of Fe_mBTC_n remained stable before 350 °C (Figure S5). As shown in Figure 3c, the peak at 161 °C in $Fe_1BTC_{0.5}$, attributed to the weak physical adsorption of *o*-xylene,[40] progressively shifts to lower temperatures of 157 °C in Fe_1BTC_1 and 145 °C in Fe_1BTC_2. Concurrently, the peak at 217 °C in $Fe_1BTC_{0.5}$ corresponds to the $\pi-\pi$ interaction between *o*-xylene molecules and benzene ring in BTC^{3-},[41,42] gradually moving toward higher temperatures of 223 °C in Fe_1BTC_1 and Fe_1BTC_2. Notably, the peak intensity follows the order of $Fe_1BTC_{0.5}$ (217 °C) > Fe_1BTC_1 (223 °C) > $Fe_1BTC_{0.5}$ (223 °C). The change is primarily due to the increased microporosity in Fe_1BTC_1 and Fe_1BTC_2 compared with $Fe_1BTC_{0.5}$, which hinders the desorption of *o*-xylene. Furthermore, the peak at 312 °C in $Fe_1BTC_{0.5}$, assigned to the Lewis acid–base interaction between the exposed Fe–O sites and *o*-xylene,[41,42] shifts to lower temperatures at 309 °C in Fe_1BTC_1 and 306 °C in Fe_1BTC_2. The above results indicate that the interaction between $Fe_1BTC_{0.5}$ and *o*-xylene is strongest among the samples and is gradually weakened with the increasing dosage of H_3BTC. Meanwhile, in Figure 3d, the results of the increasing contact angle ($Fe_1BTC_{0.5}$ ~ 20.3°, Fe_1BTC_1 ~ 21.4°, and Fe_1BTC_2 ~ 23.5°) between Fe_mBTC_n and *o*-xylene show that the affinity of Fe_mBTC_n toward *o*-xylene also decreased with the increasing dosage of H_3BTC. Combined with the results of NH_3-TPD, the gradual weakening of interaction between Fe_mBTC_n (from $Fe_1BTC_{0.5}$ to Fe_1BTC_1 and Fe_1BTC_2) and *o*-xylene is caused by the reduction of the exposure degree of Fe–O Lewis acid sites.

3.3. Density Functional Theory (DFT) Calculations.

Density functional theory (DFT) calculations were carried out to further disclose the interactions between Fe_mBTC_n and *o*-xylene. XPS, TPD, and contact angle test results confirm the exposure degree and Lewis acidity of Fe–O sites in Fe_mBTC_n following the order of $Fe_1BTC_{0.5}$ > Fe_1BTC_1 > Fe_1BTC_2. Based on the result, we constructed three different degrees of ligand deficiency that are consistent with the trend of exposure degree and Lewis acidity of Fe–O sites in Fe_mBTC_n. As shown in Figure 4a–c, the stable structures of Fe_mBTC_n are obtained and the ground-state energies ($E_{(bare)}$) of $Fe_1BTC_{0.5}$, Fe_1BTC_1, and Fe_1BTC_2 are −591.168, −733.467, and −873.294 eV by optimizing three given poscars of catalyst clusters. The energy ($E_{(C_8H_{10})}$) of the gaseous *o*-xylene molecule in a vacuum is

https://doi.org/10.1021/acsestengg.4c00949
ACS EST Engg. XXXX, XXX, XXX–XXX

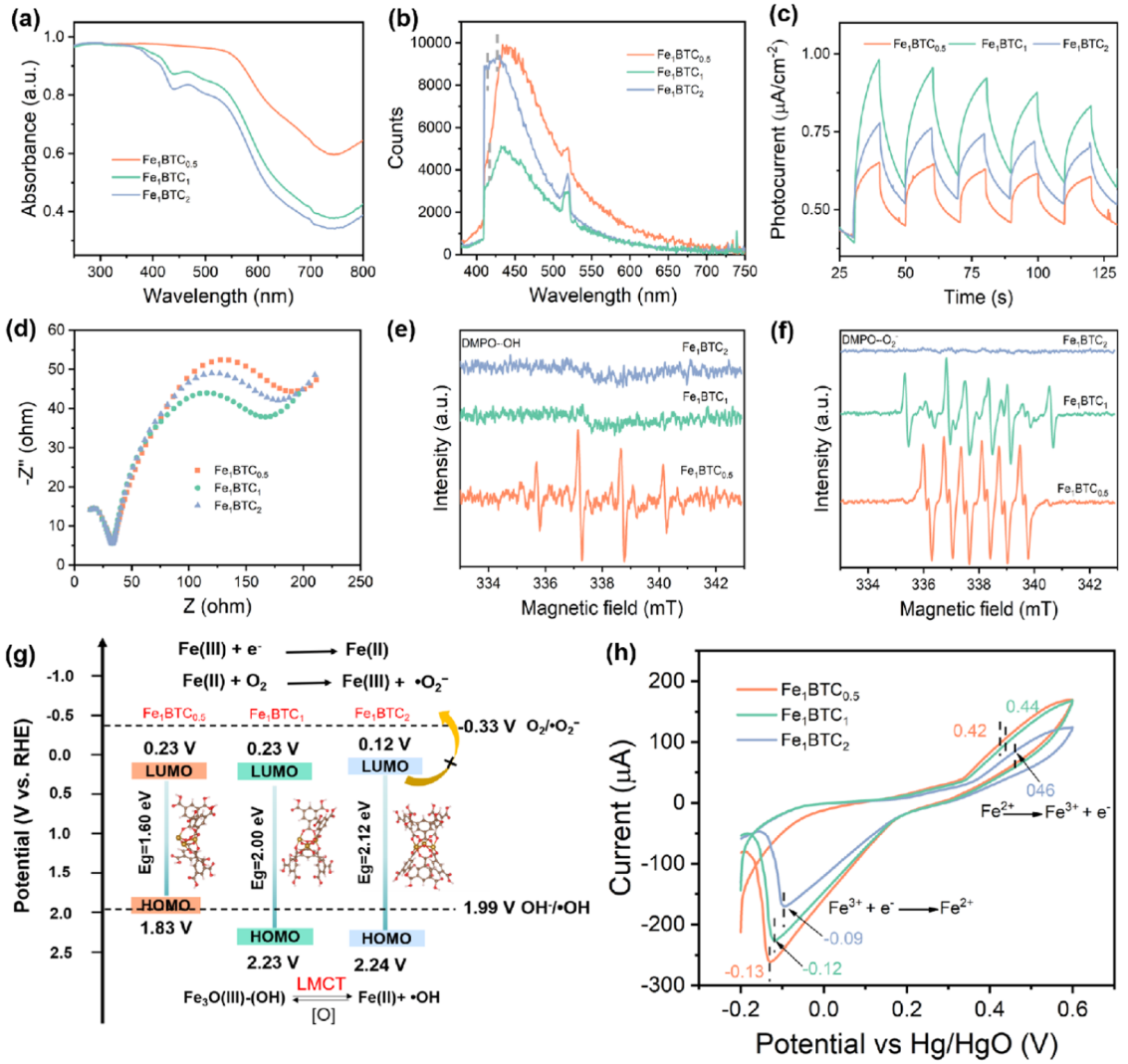

Figure 5. (a) Diffuse reflectance spectra, (b) photoluminescence spectra, (c) photocurrent response curves, and (d) electrochemical impedance spectra of Fe_mBTC_n. (e, f) DMPO spin-trapping ESR spectra for (e) ·OH and (f) $\cdot O_2^-$ of Fe_mBTC_n. (g) The estimated energy band alignments of Fe_mBTC_n. (h) CV curves of Fe_mBTC_n.

calculated as −109.420 eV. The structures of *o*-xylene adsorbed on the Fe−O Lewis acid sites and the benzene ring sites of the ligands in $Fe_1BTC_{0.5}$, Fe_1BTC_1, and Fe_1BTC_2 have been optimized and displayed in Figure 4d−i. The total energies of *o*-xylene on Fe−O Lewis acid sites ($E_{Fe(bare+C_8H_{10})}$) and the total energies of *o*-xylene on benzene ring sites ($E_{C(bare+C_8H_{10})}$) of $Fe_1BTC_{0.5}$, Fe_1BTC_1, and Fe_1BTC_2 are optimized, as shown in Tables S2 and 3.

In Figure 4d−f, the adsorption energies (ΔE) of *o*-xylene on the Fe−O Lewis acid sites in $Fe_1BTC_{0.5}$, Fe_1BTC_1, and Fe_1BTC_2 calculated by eq I are −0.791, −0.490, and −0.343 eV, respectively, more negative than that on the benzene ring sites of the ligands, which are determined as −0.500, −0.391, and 2.002 eV (Figure 4g−i), respectively. The results confirm that the adsorption ability of *o*-xylene on the Fe−O Lewis acid sites is significantly stronger than that on the benzene ring sites of the ligands and the adsorption ability gradually weakens as the exposure degree of Fe−O sites in Fe_mBTC_n decreases. The conclusion can be drawn that Lewis acid−base interaction other than $\pi-\pi$ interaction plays a predominant role during the adsorption of *o*-xylene in all samples.

$$\Delta E = E_{(bare+C_8H_{10})} - E_{(C_8H_{10})} - E_{(bare)} \quad (I)$$

3.4. Photoelectric Properties of Fe_mBTC_n. In addition to the adsorption modes, the photoelectric properties of Fe_mBTC_n also seriously affect PCO of *o*-xylene. As shown in Figure 5a, Fe_mBTC_n samples show excellent light absorption behavior in both ultraviolet and visible regions, although the visible light absorption ability of Fe_1BTC_1 and Fe_1BTC_2 decreases compared with $Fe_1BTC_{0.5}$. As shown in Figure 5b, the maximum fluorescence emission peaks of Fe_1BTC_1 and Fe_1BTC_2 are blue-shifted compared with $Fe_1BTC_{0.5}$, interpreted by the fact that Fe_1BTC_1 and Fe_1BTC_2 have more benzene ring-conjugated extended structures, which increase the electron energy level.[26] Besides, Fe_1BTC_1 shows a lower photoluminescence intensity compared with $Fe_1BTC_{0.5}$ and Fe_1BTC_2. Similarly, Fe_1BTC_1 exhibits a much higher photocurrent response compared with $Fe_1BTC_{0.5}$ and Fe_1BTC_2 in Figure 5c, which confirms that the appropriate exposure degree of Fe−O sites in Fe_1BTC_1 is beneficial for the effective trap of photogenerated electrons and prolonging the lifetime of excited electrons and holes.[43] Excessive or deficient exposure of Fe−O sites is not conducive to the short-range ordering of

https://doi.org/10.1021/acsestengg.4c00949
ACS EST Engg. XXXX, XXX, XXX−XXX

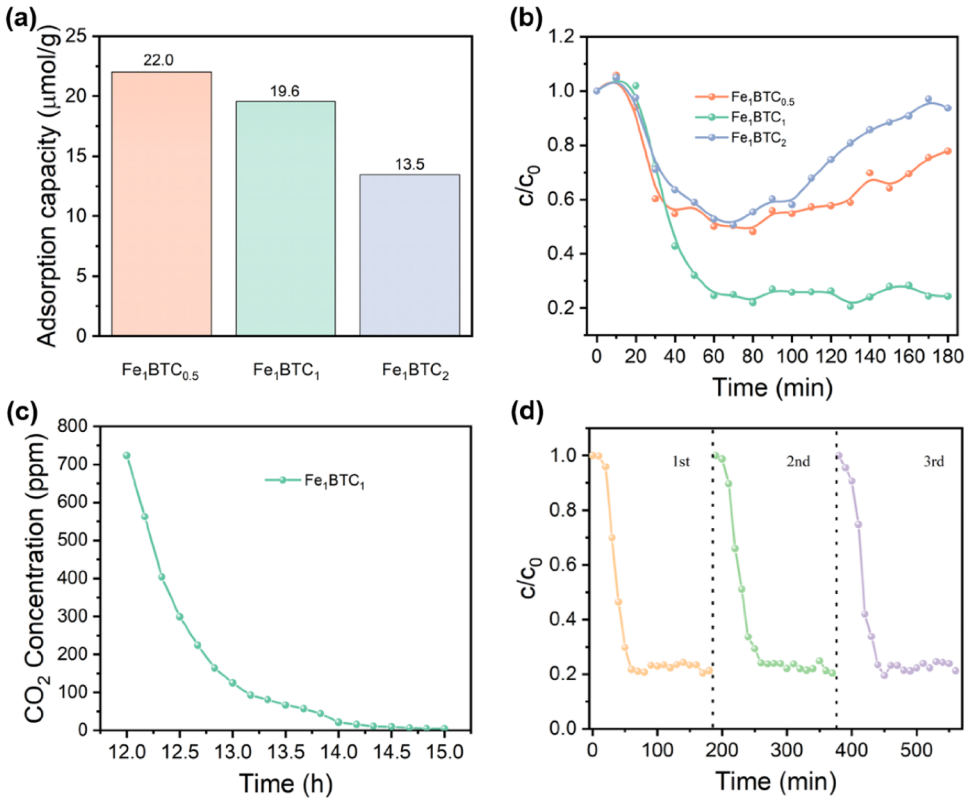

Figure 6. (a) Saturated adsorption capacities of Fe_mBTC_n on *o*-xylene. (b) The PCO efficiencies vs time curves of *o*-xylene (25 ppm) under a 250 W xenon irradiation. (c) The concentration changes of CO_2 adsorbed by Fe_1BTC_1 during PCO of *o*-xylene. (d) The durability of Fe_1BTC_1 for 3 repeated cycles for *o*-xylene (25 ppm) under a 250 W xenon lamp.

MOGs, which may be the main reason for the decrease in photoelectric properties of $Fe_1BTC_{0.5}$ and Fe_1BTC_2.[27] As shown in Figure 5d, Fe_1BTC_1 exhibits the smallest diameter semicircle compared with $Fe_1BTC_{0.5}$ and Fe_1BTC_2 in electrochemical impedance spectroscopy, which agrees with the results of photocurrent response and photoluminescence spectroscopy. To further investigate the dynamic behavior of photogenerated carriers in Fe_mBTC_n, transient fluorescence attenuation spectra were used to study the lifetime of photogenerated carriers in Figure S6. The double exponential fitting results of transient fluorescence attenuation spectra show that the average lifetime of photogenerated carriers in Fe_1BTC_1 (0.44 ns) is higher than that of $Fe_1BTC_{0.5}$ (0.42 ns) and Fe_1BTC_2 (0.43 ns). The prolonged lifetime of electrons enables their migration to the surface of the photocatalyst to participate in the oxidation of *o*-xylene. The above results indicate that the appropriate exposure degree of Fe−O sites in Fe_1BTC_1 promotes the separation of photogenerated electrons and holes and prolongs the lifetime of electrons, which is beneficial for the generation of oxidative radicals and the decomposition of adsorbed *o*-xylene.

The highest occupied molecular orbital (HOMO) level of Fe_mBTC_n (E_{HOMO}) was obtained by determining the ionization potential with ultraviolet photoelectron spectroscopy (UPS).[44,45] E_{HOMO} of $Fe_1BTC_{0.5}$, Fe_1BTC_1, and Fe_1BTC_2 are calculated to be −6.27, −6.67, and −6.68 eV (vs vacuum), respectively, according to Equation SI. As displayed in Figure S7a and b, E_{Fermi} of $Fe_1BTC_{0.5}$, Fe_1BTC_1, and Fe_1BTC_2 are 6.34, 6.77, and 7.19 eV, and E_{cutoff} are 21.29, 21.32, and 21.73 eV, respectively. According to the relationship between the vacuum energy (E_{vacuum}) and the RHE potential (E_{RHE}) (eq SII), E_{HOMO} of $Fe_1BTC_{0.5}$, Fe_1BTC_1, and Fe_1BTC_2 vs RHE are calculated as 1.83, 2.23, and 2.24 V, which are lower than that of XPS (Figure S8) due to the maximum HOMO of the samples given by XPS.[46] The band gap values of $Fe_1BTC_{0.5}$, Fe_1BTC_1, and Fe_1BTC_2 are 1.60, 2.00, and 2.12 eV obtained from UV−vis spectra (Figure S9). The low occupied molecular orbital levels (E_{LUMO}) of $Fe_1BTC_{0.5}$, Fe_1BTC_1, and Fe_1BTC_2 vs RHE are determined to be 0.23, 0.23, and 0.12 V by eq SIII. As shown in Figure 5e and f, hydroxyl radical (·OH) and superoxide radical ($\cdot O_2^-$) are observed in $Fe_1BTC_{0.5}$, and only $\cdot O_2^-$ is found in Fe_1BTC_1 and Fe_1BTC_2. The intensity of $\cdot O_2^-$ generated in Fe_1BTC_1 is significantly higher than that of Fe_1BTC_2 under light irradiation. These are not completely matched with their E_{HOMO} and E_{LUMO} vs RHE. On the one hand, Fe_3O-(OH) sites are formed in $Fe_1BTC_{0.5}$ due to more water molecules adsorbed on its highly exposed Fe−O Lewis acid sites. Then an inner ligand−metal charge transfer (LMCT)[47,48] happens on Fe_3O-(OH) sites for the oxidation of OH-/·OH (1.99 eV vs NHE) in Figure 5g. Fe_1BTC_1 and Fe_1BTC_2 with appropriate and low exposure degree of Fe−O Lewis acid sites prevent adsorbed water to form Fe_3O-(OH) sites and inhibit the generation of ·OH through LMCT. On the other hand, electrons generated at the LUMO level transfer to the HOMO level under the excitation of light, and Fe(III) in the exposed Fe−O Lewis acid sites is reduced to Fe(II),[49] which is further oxidized to Fe(III) with the generation of $\cdot O_2^-$. The result is confirmed by the CV curves exhibiting cyclic conversion of Fe(III) and Fe(II) in Figure 5h. The intensities of $\cdot O_2^-$ produced by Fe_mBTC_n are $Fe_1BTC_{0.5}$ > Fe_1BTC_1 > Fe_1BTC_2, agreed with the exposure degree of Fe−O Lewis acid sites of Fe_mBTC_n ($Fe_1BTC_{0.5}$ > Fe_1BTC_1 > Fe_1BTC_2).

https://doi.org/10.1021/acsestengg.4c00949
ACS EST Engg. XXXX, XXX, XXX−XXX

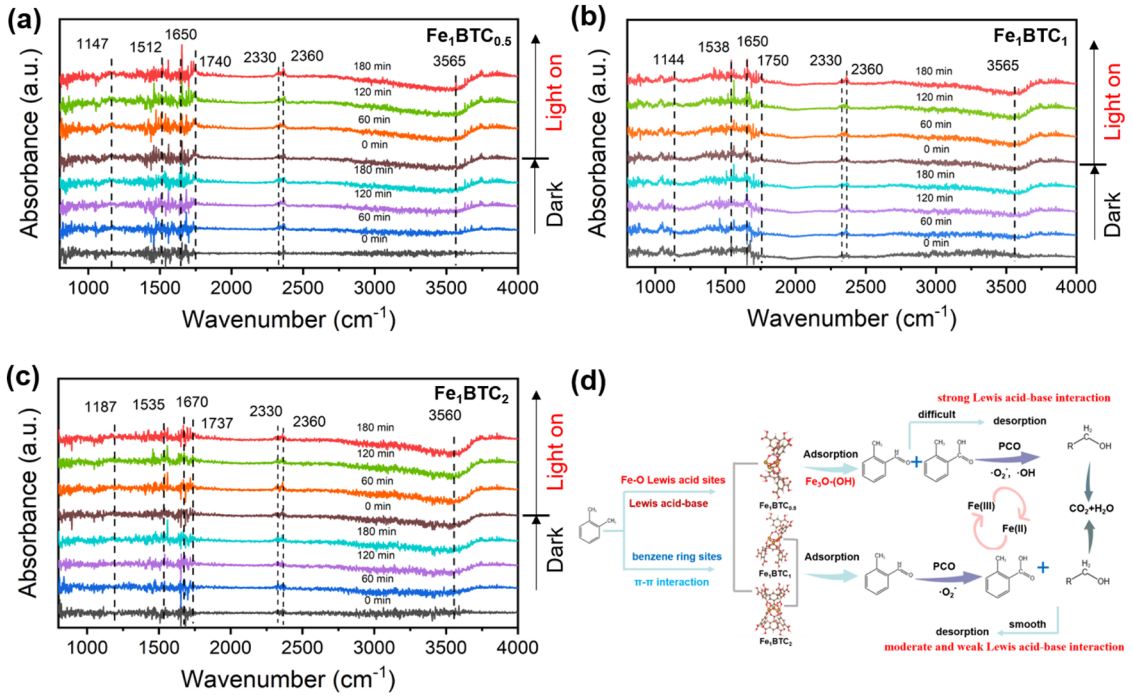

Figure 7. (a–c) *In situ* DRIFT spectra of (a) $Fe_1BTC_{0.5}$, (b) Fe_1BTC_1, and (c) Fe_1BTC_2 during the adsorption and PCO of *o*-xylene. (d) The pathways of PCO of *o*-xylene by Fe_mBTC_n.

3.5. Adsorption and PCO Performance of *o*-Xylene. *O*-xylene was used as the target pollutant to test the ability of Fe_mBTC_n in PCO of aromatic VOCs. First, adsorption experiments were performed to shed light on the influence of the exposure degree of Fe−O sites in Fe_mBTC_n on their adsorption capacity for *o*-xylene. As shown in Figure S10, when Fe_mBTC_n is applied, the real-time concentrations of *o*-xylene are much lower than those in the blank chamber, demonstrating that *o*-xylene molecules are effectively adsorbed by Fe_mBTC_n. The adsorption capacity of Fe_mBTC_n for *o*-xylene calculated by eq SIV is displayed in Figure 6a. $Fe_1BTC_{0.5}$ with the lowest NLDFT cumulative surface area shows the highest adsorption capacity (22.0 μmol/g) for *o*-xylene due to the highest exposure degree of Fe−O sites and benzene ring sites in ligands, both exhibiting the most negative adsorption energy to *o*-xylene. Compared with $Fe_1BTC_{0.5}$, Fe_1BTC_1 and Fe_1BTC_2 display higher NLDFT cumulative surface areas, but the adsorption capacities for *o*-xylene decrease to 19.6 and 13.5 μmol/g, respectively, which is attributed to the lower exposure degree of Fe−O sites and benzene ring sites in ligands, as well as the relatively positive adsorption energies to *o*-xylene.[50] The results confirm that the high exposure degrees of Fe−O Lewis acid sites and benzene ring sites of ligands promote together the adsorption of *o*-xylene. PCO of *o*-xylene was subsequently carried out under a 250 W xenon irradiation. As shown in Figure 6b, the efficiencies of $Fe_1BTC_{0.5}$ and Fe_1BTC_2 in oxidizing *o*-xylene are 52 and 49%, respectively, according to eq SV. The PCO efficiency of $Fe_1BTC_{0.5}$ and Fe_1BTC_2 toward *o*-xylene gradually declined as the reaction lasted for 80 min. When the reaction time reached 180 min, the PCO efficiency of $Fe_1BTC_{0.5}$ dropped from 52 to 22%, while that of Fe_1BTC_2 decreased from 49 to 6%, respectively. The reason for the decreased PCO performance of $Fe_1BTC_{0.5}$ is that the generation and accumulation of intermediates, formed by the rapid oxidation of *o*-xylene under high intensities of ·OH and $\cdot O_2^-$, covered the exposed Fe−O catalytic active sites.[23,29] Besides, the highly exposed Fe−O Lewis acid catalytic sites display strong adsorption ability for *o*-xylene and benzyl midproducts, hindering the separation of intermediates from the catalytic active sites in a timely manner. Different from $Fe_1BTC_{0.5}$, Fe_1BTC_2 only produces a low intensity of $\cdot O_2^-$ due to the low exposure of Fe−O catalytic sites, which is unable to effectively oxidize *o*-xylene molecules, resulting in a decrease in the PCO performance for Fe_1BTC_2.[51] The oxidation efficiency of Fe_1BTC_1 toward *o*-xylene reaches 80% and maintains considerable activity for 180 min, higher than that of $Fe_1BTC_{0.5}$ and Fe_1BTC_2, which is also advantageous compared with previously discovered photocatalysts (Table S4). This is related to the oxidation of *o*-xylene by high intensity of $\cdot O_2^-$ generated. Meantime, the abundant mesopore channels in Fe_1BTC_1 impair the Lewis acid−base interaction between intermediates and Fe−O catalytic sites, allowing them to be smoothly removed from the active sites. In brief, the exposure degree of Fe−O sites and photoelectric properties in Fe_mBTC_n show a synergistic effect in PCO of *o*-xylene. The CO_2 generated during PCO of *o*-xylene was tested using GC-FID with a graphite conversion furnace. CO_2 was not detected during the photocatalytic process. After the photocatalytic reaction was completed, the entire reaction system was sealed for 12 h, and CO_2 was detected (Figure 6c), which was probably that the generation of CO_2 was intercepted in the pore channels during PCO and gradually escaped from the surface of Fe_1BTC_1 with the time. The specific detection method has been described in detail in previous articles.[23] The efficiency of Fe_1BTC_1 in converting *o*-xylene to CO_2 was 67.5% by integral calculation. The stability and durability of Fe_1BTC_1 in PCO of *o*-xylene were studied by cyclic experiments. As shown in Figure 6d, the PCO efficiency of Fe_1BTC_1 remains at 80% after 3 cycles.

3.6. Mechanism of PCO of *o*-Xylene. The evolution of the intermediates produced on Fe_mBTC_n during adsorption and PCO of *o*-xylene was detected by *in situ* DRIFT spectra.

https://doi.org/10.1021/acsestengg.4c00949
ACS EST Engg. XXXX, XXX, XXX−XXX

The testing conditions used for introducing *o*-xylene into the DRIFT cell, including the flow rate of *o*-xylene and air, were consistent with those of the photocatalytic performance. The *in situ* DRIFT spectrometer was set to collect spectra every 30 min, as shown in Figure 7, to discuss the adsorption and PCO process. In Figure 7a, the access time of *o*-xylene lasts for 180 min until the DRIFT spectra remain stable during which $Fe_1BTC_{0.5}$ reaches adsorption equilibrium. From the spectrum at 180 min, the negative peak at 3565 cm^{-1} is assigned to the O−H stretching vibration of surface-adsorbed water. The peak at 1512 cm^{-1} is associated with the vibration of the benzene ring skeleton, indicating that *o*-xylene molecules are successfully adsorbed on the surface of $Fe_1BTC_{0.5}$.[52,53] The peak at 1650 cm^{-1} corresponding to the stretching vibration of C = O in the benzaldehydes is observed and the peak intensity increased with the prolongation of adsorption time.[52,53] When the adsorption time carries on 120 min, the peak of 1740 cm^{-1} attributed to the carboxyl groups is discovered.[6,54] The assumption is that the α-H of *o*-xylene first interacts with the exposed Fe−O Lewis sites to form benzaldehydes, which is further oxidized to benzoic acids as the adsorption proceeds.[55] After turning on the xenon lamp, the peaks at 1650, 1740, and 3565 cm^{-1} become more and more intense, while the peak at 1147 cm^{-1} assigned to C−O in aliphatic alcohols is found, confirming the successive ring opening of benzaldehydes or benzoic acids is attacked by ·OH and $\cdot O_2^-$ generated from $Fe_1BTC_{0.5}$. Besides, the intensities of peaks at 2330 and 2360 cm^{-1} ascribed to asymmetric stretching vibration of C = O in CO_2 are also significantly increased. Therefore, the intermediates produced during PCO of *o*-xylene, such as benzaldehydes, benzoic acids, and aliphatic alcohols, are deeply oxidized to CO_2 by ·OH and $\cdot O_2^-$.

In Figure 7b and c, unlike the adsorption of *o*-xylene by $Fe_1BTC_{0.5}$, only the vibration peaks of benzene ring skeleton (1538 cm^{-1} in Fe_1BTC_1 and 1535 cm^{-1} in Fe_1BTC_2) and benzaldehydes (1650 cm^{-1} in Fe_1BTC_1 and 1670 cm^{-1} in Fe_1BTC_2) are found, which is closely related to the decrease in the exposure degree of Fe−O sites. When the illumination time lasts for 60 min, the peaks of aliphatic alcohols (1144 cm^{-1}) and benzoic acids (1750 cm^{-1}) on the surface of Fe_1BTC_1 are observed, while the peaks of aliphatic alcohols (1187 cm^{-1}) and benzoic acids (1737 cm^{-1}) on the surface of Fe_1BTC_2 are found as the illumination time reached 120 min, indicating that the oxidation ability of Fe_1BTC_1 is stronger than that of Fe_1BTC_2, which corresponds to a higher intensity of $\cdot O_2^-$ generated by Fe_1BTC_1 higher than Fe_1BTC_2. Compared with $Fe_1BTC_{0.5}$, the peak of benzoic acids (1740 cm^{-1}) has already appeared under the action of exposed Fe−O sites in the process of adsorbing *o*-xylene, and when the light is turned on, the peak of aliphatic alcohols (1147 cm^{-1}) immediately is observed, accompanied by a significant increase in the peak intensity of benzoic acids (1740 cm^{-1}). This confirms that the high intensity of ·OH produced by $Fe_1BTC_{0.5}$ with the highly exposed Fe−O Lewis acid sites is essential for the ring opening of *o*-xylene. In addition, the peak intensity of benzaldehydes at 1650 cm^{-1} in $Fe_1BTC_{0.5}$ is significantly higher than that of other samples (1650 cm^{-1} in Fe_1BTC_1 and 1670 cm^{-1} in Fe_1BTC_2), which further confirms the accumulation of aromatic intermediates.

The pathways of PCO of *o*-xylene by Fe_mBTC_n are suggested in Figure 7d according to *in situ* DRIFT spectra. First, *o*-xylene molecules are adsorbed on the exposed Fe−O and benzene ring sites in the ligand of Fe_mBTC_n through Lewis acid−base and $\pi-\pi$ interactions. $Fe_1BTC_{0.5}$ with highly exposed Fe−O sites convert *o*-xylene to benzaldehydes and benzoic acids by attacking α-H of *o*-xylene, while Fe_1BTC_1 and Fe_1BTC_2 with appropriate and low exposure degree of Fe−O sites only transform *o*-xylene to benzaldehydes. Under light irradiation conditions, the ring-opening reaction of benzaldehydes and benzoic acids occurs on $Fe_1BTC_{0.5}$ with high intensity of ·OH and $\cdot O_2^-$ to produce aliphatic alcohols. However, a large amount of intermediates cannot be removed in time from the exposed Fe−O sites due to their strong adsorption ability for benzyl species, resulting in a decrease in the PCO performance of $Fe_1BTC_{0.5}$. Benzaldehydes on the surface of Fe_1BTC_1 are transformed into benzoic acids by the high intensity of $\cdot O_2^-$ generated by the appropriate exposure degree of Fe−O sites. Benefiting from the moderate adsorption ability for *o*-xylene in Fe_1BTC_1, the intermediates are allowed to leave smoothly from catalytic sites and make Fe_1BTC_1 display excellent and stable oxidation ability for *o*-xylene. The low intensity of $\cdot O_2^-$ is generated by the low exposure degree of Fe−O sites in Fe_1BTC_2, which prevents the subsequent oxidation of benzaldehydes and results in a lower oxidation efficiency to *o*-xylene.

4. CONCLUSIONS

A series of Fe-MOGs with Fe−O sites of different exposure degrees and Lewis acidity have been successfully prepared. The results of XPS, NH_3-TPD, and contact angle confirm that the exposure degree and Lewis acidity of Fe−O sites in Fe_mBTC_n gradually decrease with the increase of H_3BTC added ($Fe_1BTC_{0.5}$ > Fe_1BTC_1 > Fe_1BTC_2). The highly exposed Fe−O sites with strong Lewis acidity not only enable the effective adsorption of *o*-xylene molecules by oxidizing them into benzaldehydes and benzoic acids but also promote the generation of oxidative radicals for the ring opening of *o*-xylene. A balance between the exposure of Fe−O sites and the photoelectric properties of Fe_mBTC_n is necessary. On the one hand, despite the improved adsorption capacity toward *o*-xylene, highly exposed Fe−O sites will strongly capture the intermediates, leading to a decrease in the PCO performance of the sample. On the other hand, the low exposure degree of Fe−O sites detriments the generation of oxidative radicals owing to the lack of active OMSs. Owing to the appropriate exposure degree of Fe−O sites and excellent photoelectric properties, Fe_1BTC_1 shows not only improved efficiency (80%) but also higher stability (180 min) during PCO of *o*-xylene than $Fe_1BTC_{0.5}$ (52%, 80 min) and Fe_1BTC_2 (49%, 80 min). Our results confirm the possibility of modulating the PCO reaction paths of VOCs through regulating the active sites of photocatalysts and shed light on the controllable conversion of VOCs to high-value products.

■ ASSOCIATED CONTENT

Supporting Information

The Supporting Information is available free of charge at https://pubs.acs.org/doi/10.1021/acsestengg.4c00949.

Preparation of samples; Materials characterization; The calculation formulas of E_{HOMO} and E_{LUMO}; Performance evaluation of Fe_mBTC_n; NH_3/*o*-xylene-TPD; Density functional theory (DFT) calculations; Process diagram of photocatalytic oxidation reaction system; XRD pattern of stimulated MIL-100(Fe); SEM images of Fe_mBTC_n and EDS mappings of C, Fe, and O elements

https://doi.org/10.1021/acsestengg.4c00949
ACS EST Engg. XXXX, XXX, XXX−XXX

of Fe_1BTC_1; XPS survey spectra of Fe_mBTC_n; TG curves of Fe_mBTC_n in N_2; The transient fluorescence attenuation spectra of Fe_mBTC_n; UPS spectra; The HOMO-XPS of Fe_mBTC_n; The plots of $(\alpha h\nu)^2$ vs photon energy $(h\nu)$ of Fe_mBTC; The adsorption curves of *o*-xylene on Fe_mBTC_n; The fitting peak area proportion of O 1s in Fe_mBTC_n; The adsorption energies of *o*-xylene on the Fe−O Lewis acid sites; The adsorption energies of *o*-xylene on the benzene ring sites in ligands; Comparison of the PCO performance of *o*-xylene on different catalysis in the same test equipment (PDF)

AUTHOR INFORMATION

Corresponding Authors

Xiao Wang − *State Key Lab of High Performance Ceramics and Superfine Microstructure, Shanghai Institute of Ceramics, Chinese Academy of Sciences, Shanghai 201899, China;* orcid.org/0000-0001-9786-8153; Email: wangxiao@mail.sic.ac.cn

Jing Sun − *State Key Lab of High Performance Ceramics and Superfine Microstructure, Shanghai Institute of Ceramics, Chinese Academy of Sciences, Shanghai 201899, China;* orcid.org/0000-0003-1101-1584; Email: jingsun@mail.sic.ac.cn

Deliang Chen − *Research Institute of Interdisciplinary Science & School of Materials Science and Engineering, Dongguan University of Technology, Dongguan 523808, China;* orcid.org/0000-0002-2076-8733; Email: dlchen@zzu.edu.cn

Authors

Lu Chen − *Research Institute of Interdisciplinary Science & School of Materials Science and Engineering, Dongguan University of Technology, Dongguan 523808, China; Institute of Fundamental and Frontier Sciences, University of Electronic Science and Technology of China, Chengdu 611731, China*

Guanqing Song − *State Key Lab of High Performance Ceramics and Superfine Microstructure, Shanghai Institute of Ceramics, Chinese Academy of Sciences, Shanghai 201899, China*

Chi Song − *State Key Lab of High Performance Ceramics and Superfine Microstructure, Shanghai Institute of Ceramics, Chinese Academy of Sciences, Shanghai 201899, China*

Haijiao Xie − *Hangzhou Yanqu Information Technology Co., Ltd., Hangzhou 310003, China*

Fan Dong − *Institute of Fundamental and Frontier Sciences, University of Electronic Science and Technology of China, Chengdu 611731, China;* orcid.org/0000-0003-2890-9964

Complete contact information is available at: https://pubs.acs.org/10.1021/acsestengg.4c00949

Author Contributions

CRediT: **Lu Chen** conceptualization, data curation, formal analysis, funding acquisition, investigation, methodology, project administration, supervision, writing - original draft; **Guanqing Song** data curation, formal analysis, methodology; **Xiao Wang** conceptualization, formal analysis, methodology, supervision, writing - review & editing; **Chi Song** formal analysis, software, supervision; **Xie Haijiao** methodology, software, visualization; **Jing Sun** conceptualization, funding acquisition, project administration, supervision, writing - review & editing; **Fan Dong** supervision, writing - review & editing; **Deliang Chen** conceptualization, funding acquisition, methodology, project administration, supervision, writing - review & editing.

Notes

The authors declare no competing financial interest.

ACKNOWLEDGMENTS

This work was financially supported by the National Natural Science Foundation of China (52072387), the China Postdoctoral Science Foundation (2023M740514), the Basic and Applied Basic Research Foundation of Guangdong Province (2021B1515140047 and 2023A1515110680), the Guangdong Provincial Key Construction Discipline Research Ability Enhancement Project (2021ZDJS090), the Dongguan Science and Technology of Social Development Program (20221800905122), and the Key Scientific Research Project in the University of Henan Province (21A430040).

REFERENCES

(1) Barea, E.; Montoro, C.; Navarro, J. A. R. Toxic gas removal-metal-organic frameworks for the capture and degradation of toxic gases and vapours. *Chem. Soc. Rev.* **2014**, *43* (16), 5419−5430.

(2) Wen, M.; Li, G.; Liu, H.; Chen, J.; An, T.; Yamashita, H. Metal-organic framework-based nanomaterials for adsorption and photocatalytic degradation of gaseous pollutants: recent progress and challenges. *Environ. Sci. Nano.* **2019**, *6* (4), 1006−1025.

(3) Qu, W.; Xu, Z.; Gruber, C. G.; Li, H.; Hu, X.; Zhou, L.; Duan, H.; Zhang, J.; Liu, M.; Cortés, E.; Zhang, D. Accelerating Toluene Oxidation over Boron-Titanium-Oxygen Interface: Steric Hindrance of the Methyl Group Induced by the Plane-Adsorption Configuration. *Environ. Sci. Technol.* **2024**, *58* (36), 16215−16224.

(4) Zhang, J.; Vikrant, K.; Kim, K.-H.; Dong, F.; Won Chung, M.; Weon, S. Unveiling the collective effects of moisture and oxygen on the photocatalytic degradation of m-Xylene using a titanium dioxide supported platinum catalyst. *Chem. Eng. J.* **2022**, *439*, No. 135747.

(5) Chen, L.; Li, K.; Yang, Y.; Xue, T.; Wang, H.; Lei, B.; Sheng, J.; Dong, F.; Sun, Y. Amorphous SnO_2 decorated $ZnSn(OH)_6$ promotes interfacial hydroxyl polarization for deep photocatalytic toluene mineralization. *J. Hazard. Mater.* **2023**, *444*, No. 130436.

(6) Rao, Z.; Lu, G.; Mahmood, A.; Shi, G.; Xie, X.; Sun, J. Deactivation and activation mechanism of TiO_2 and rGO/Er^{3+}-TiO_2 during flowing gaseous VOCs photodegradation. *Appl. Catal., B* **2021**, *284*, No. 119813.

(7) Hou, J.; Sapnik, A. F.; Bennett, T. D. Metal-organic framework gels and monoliths. *Chem. Sci.* **2020**, *11* (2), 310−323.

(8) Wychowaniec, J. K.; Saini, H.; Scheibe, B.; Dubal, D. P.; Schneemann, A.; Jayaramulu, K. Hierarchical porous metal-organic gels and derived materials: from fundamentals to potential applications. *Chem. Soc. Rev.* **2022**, *51* (21), 9068−9126.

(9) Zhuang, Z.; Mai, Z.; Wang, T.; Liu, D. Strategies for conversion between metal-organic frameworks and gels. *Coord. Chem. Rev.* **2020**, *421*, No. 213461.

(10) Draper, E. R.; Adams, D. J. Controlling supramolecular gels. *Nat. Mater.* **2024**, *23* (1), 13−15.

(11) Rostami, J.; Benselfelt, T.; Maddalena, L.; Avci, C.; Sellman, F. A.; Cinar Ciftci, G.; Larsson, P. A.; Carosio, F.; Akhtar, F.; Tian, W.; Wågberg, L. Shaping 90 wt% NanoMOFs into Robust Multifunctional Aerogels Using Tailored Bio-Based Nanofibrils. *Adv. Mater.* **2022**, *34* (38), No. 2204800.

(12) Qin, H.; Li, N.; Xu, H.-M.; Guo, Q.-Y.; Cong, H.-P.; Yu, S.-H. Double Confinement Hydrogel Network Enables Continuously Regenerative Solar-to-Hydrogen Conversion. *Angew. Chem., Int. Ed.* **2022**, *61* (42), No. e202209687.

(13) Yang, Z.; Fu, X.; Zhou, L.; Yang, J.; Deng, T.; Chen, J.; Wen, Y.; Fu, X.; Shen, D.; Yuan, Z.; Du, Z.; Luo, S.; Yu, C. Chem-inspired synthesis of injectable metal-organic hydrogels for programmable drug carriers, hemostasis and synergistic cancer treatment. *Chem. Eng. J.* **2021**, *423*, No. 130202.
(14) Ji, K.; Xia, S.; Sang, X.; Zeid, A. M.; Hussain, A.; Li, J.; Xu, G. Enhanced Luminol Chemiluminescence with Oxidase-like Properties of FeOOH Nanorods for the Sensitive Detection of Uric Acid. *Anal. Chem.* **2023**, *95* (6), 3267−3273.
(15) Cowie, B. E.; Mears, K. L.; S'ari, M.; Lee, J. K.; Briceno de Gutierrez, M.; Kalha, C.; Regoutz, A.; Shaffer, M. S. P.; Williams, C. K. Exploiting Organometallic Chemistry to Functionalize Small Cuprous Oxide Colloidal Nanocrystals. *J. Am. Chem. Soc.* **2024**, *146* (6), 3816−3824.
(16) Whitaker, T.; Tuttle, R.; Thai, J. E.; Schwarz, M. C. R.; Reynolds, M. M. Copper(II) Ions Originating from CuBTC MOF Act as a Soluble Catalyst in the Friedländer Synthesis. *ACS Appl. Mater. Interfaces* **2024**, *16* (17), 22641−22647.
(17) Li, P.; Kim, S.; Jin, J.; Do, H. C.; Park, J. H. Efficient photodegradation of volatile organic compounds by iron-based metal-organic frameworks with high adsorption capacity. *Appl. Catal., B* **2020**, *263*, No. 118284.
(18) Liu, Y.; Klet, R. C.; Hupp, J. T.; Farha, O. Probing the correlations between the defects in metal−organic frameworks and their catalytic activity by an epoxide ring-opening reaction. *Chem. Commun.* **2016**, *52* (50), 7806−7809.
(19) Jin, J.; Li, P.; Chun, D. H.; Jin, B.; Zhang, K.; Park, J. H. Defect Dominated Hierarchical Ti-Metal-Organic Frameworks via a Linker Competitive Coordination Strategy for Toluene Removal. *Adv. Funct. Mater.* **2021**, *31*, No. 2102511.
(20) Yu, J.; Wang, X.; Chen, L.; Lu, G.; Shi, G.; Xie, X.; Wang, Y.; Sun, J. Enhanced adsorption and visible-light photocatalytic degradation of toluene by CQDs/UiO-66 MOG with hierarchical pores. *Chem. Eng. J.* **2022**, *435*, No. 135033.
(21) Dai, S.; Simms, C.; Patriarche, G.; Daturi, M.; Tissot, A.; Parac-Vogt, T. N.; Serre, C. Highly defective ultra-small tetravalent MOF nanocrystals. *Nat. Commun.* **2024**, *15* (1), No. 3434.
(22) Chen, L.; Wang, X.; Rao, Z.; Tang, Z.; Shi, G.; Wang, Y.; Lu, G.; Xie, X.; Chen, D.; Sun, J. One-pot Synthesis of the MIL-100 (Fe) MOF/MOX Homojunctions with Tunable Hierarchical Pores for the Photocatalytic Removal of BTXS. *Appl. Catal., B* **2022**, *303*, No. 120885.
(23) Chen, L.; Wang, X.; Shi, G.; Lu, G.; Wang, Y.; Xie, X.; Chen, D.; Sun, J. The regulation of Lewis acid/basic sites in NaFe bimetal MOXs for the controllable photocatalytic degradation of electron-rich/deficient VOCs. *Appl. Catal., B* **2023**, *334*, No. 122850.
(24) Tang, Z.; Tao, H.; Wang, X.; Chen, L.; Song, C.; Lu, G.; Xie, X.; Sun, J. Quasi-In Situ Synthesis of Ag NPs@m-MIL-100(Fe) for the Enhanced Photocatalytic Elimination of Flowing Xylenes. *ACS Appl. Mater. Interfaces* **2022**, *14* (47), 52894−52906.
(25) Xia, Q.; Wang, H.; Huang, B.; Yuan, X.; Zhang, J.; Zhang, J.; Jiang, L.; Xiong, T.; Zeng, G. State-of-the-Art Advances and Challenges of Iron-Based Metal Organic Frameworks from Attractive Features, Synthesis to Multifunctional Applications. *Small* **2019**, *15* (2), No. e1803088.
(26) Zhang, H.; Si, S.; Zhai, G.; Li, Y.; Liu, Y.; Cheng, H.; Wang, Z.; Wang, P.; Zheng, Z.; Dai, Y.; Liu, T. X.; Huang, B. The long-distance charge transfer process in ferrocene-based MOFs with FeO_6 clusters boosts photocatalytic CO_2 chemical fixation. *Appl. Catal., B* **2023**, *337*, No. 122909.
(27) Li, B.; Xiao, D.; Deng, D.; Ye, H.; Zhou, Q.; Tang, L. A metal-organic gel based on Fe(iii) and bi-pyridine ligand for template synthesis of core/shell composite polymer nanowires. *Soft Matter* **2018**, *14* (43), 8764−8770.
(28) Mahmood, A.; Xia, W.; Mahmood, N.; Wang, Q.; Zou, R. Hierarchical Heteroaggregation of Binary Metal-Organic Gels with Tunable Porosity and Mixed Valence Metal Sites for Removal of Dyes in Water. *Sci. Rep.* **2015**, *5* (1), No. 10556.
(29) Chen, R.; Li, J.; Sheng, J.; Cui, W.; Dong, X.; Chen, P.; Wang, H.; Sun, Y.; Dong, F. Unveiling the unconventional roles of methyl number on the ring-opening barrier in photocatalytic decomposition of benzene, toluene and *o*-xylene. *Appl. Catal., B* **2020**, *278*, No. 119318.
(30) Liu, X.; Zhang, X.; Dufresne, M.; Wang, T.; Wu, L.; Lara, R.; Seco, R.; Monge, M.; Yáñez-Serrano, A. M.; Gohy, M.; Petit, P.; Chevalier, A.; Vagnot, M. P.; Fortier, Y.; Baudic, A.; Ghersi, V.; Gille, G.; Lanzi, L.; Gros, V.; Simon, L.; Héllen, H.; Reimann, S.; Le Bras, Z.; Müller, M. J.; Beddows, D.; Hou, S.; Shi, Z.; Harrison, R. M.; Bloss, W.; Dernie, J.; Sauvage, S.; Hopke, P. K.; Duan, X.; An, T.; Lewis, A. C.; Hopkins, J. R.; Liakakou, E.; Mihalopoulos, N.; Zhang, X.; Alastuey, A.; Querol, X.; Salameh, T. Measurement report: Exploring the variations in ambient BTEX in urban Europe and their environmental health implications. *Atmos. Chem. Phys.* **2025**, *25* (1), 625−638.
(31) Fu, J. H.; Zhong, Z.; Xie, D.; Guo, Y. J.; Kong, D. X.; Zhao, Z. X.; Zhao, Z. X.; Li, M. SERS-Active MIL-100(Fe) Sensory Array for Ultrasensitive and Multiplex Detection of VOCs. *Angew. Chem., Int. Ed.* **2020**, *59* (46), 20489−20498.
(32) Horcajada, P.; Surblé, S.; Serre, C.; Hong, D.-Y.; Seo, Y.-K.; Chang, J.-S.; Grenèche, J.-M.; Margiolaki, I.; Férey, G. Synthesis and catalytic properties of MIL-100(Fe), an iron(iii) carboxylate with large pores. *Chem. Commun.* **2007**, 2820−2822.
(33) Han, X.; Zhang, T.; Wang, X.; Zhang, Z.; Li, Y.; Qin, Y.; Wang, B.; Han, A.; Liu, J. Hollow mesoporous atomically dispersed metal-nitrogen-carbon catalysts with enhanced diffusion for catalysis involving larger molecules. *Nat. Commun.* **2022**, *13* (1), No. 2900.
(34) He, T.; Kong, X.-J.; Bian, Z.-X.; Zhang, Y.-Z.; Si, G.-R.; Xie, L.-H.; Wu, X.-Q.; Huang, H.; Chang, Z.; Bu, X.-H.; Zaworotko, M. J.; Nie, Z.-R.; Li, J.-R. Trace removal of benzene vapour using double-walled metal-dipyrazolate frameworks. *Nat. Mater.* **2022**, *21* (6), 689−695.
(35) Kong, M.; Wei, W.; Wang, W.; Chen, H.; He, J. A novel metal organic gel with superior oxidase-like activity for efficient and sensitive chemiluminescence detection of uric acid. *Spectrochim. Acta A Mol. Biomol. Spectrosc.* **2021**, *257*, No. 119773.
(36) Tan, Y. C.; Zeng, H. C. Lewis basicity generated by localised charge imbalance in noble metal nanoparticle-embedded defective metal-organic frameworks. *Nat. Commun.* **2018**, *9* (1), No. 4326.
(37) Zhou, J.; Dou, Y.; Wu, X. Q.; Zhou, A.; Shu, L.; Li, J. R. Alkali-Etched Ni(II)-Based Metal-Organic Framework Nanosheet Arrays for Electrocatalytic Overall Water Splitting. *Small* **2020**, *16* (41), No. e1906564.
(38) Topsøe, N.-Y.; Pedersen, K.; Derouane, E. G. Infrared and temperature-programmed desorption study of the acidic properties of ZSM-5-type zeolites. *J. Catal.* **1981**, *70* (1), 41−52.
(39) Tang, Z.; Yang, D.; Guo, H.; Lin, S.; Wang, Z. L. Spontaneous Wetting Induced by Contact-Electrification at Liquid−Solid Interface. *Adv. Mater.* **2024**, *36*, No. 2400451.
(40) Zhang, X.; Shi, X.; Chen, J.; Yang, Y.; Lu, G. The preparation of defective UiO-66 metal organic framework using MOF-5 as structural modifier with high sorption capacity for gaseous toluene. *J. Environ. Chem. Eng.* **2019**, *7* (5), No. 103405.
(41) Chen, Z.; Fang, P.; Li, J.; Han, X.; Huang, W.; Cui, W.; Liu, Z.; Warren, M. R.; Allan, D.; Cheng, P.; Yang, S.; Shi, W. Rapid extraction of trace benzene by a crown-ether-based metal-organic framework. *Natl. Sci. Rev.* **2024**, *11* (12), No. nwae342.
(42) Mukherjee, S.; Sensharma, D.; Qazvini, O. T.; Dutta, S.; Macreadie, L. K.; Ghosh, S. K.; Babarao, R. Advances in adsorptive separation of benzene and cyclohexane by metal-organic framework adsorbents. *Coord. Chem. Rev.* **2021**, *437*, No. 213852.
(43) Choi, J. Y.; Check, B.; Fang, X.; Blum, S.; Pham, H. T. B.; Tayman, K.; Park, J. Photocatalytic Hydrogen Peroxide Production through Functionalized Semiconductive Metal-Organic Frameworks. *J. Am. Chem. Soc.* **2024**, *146* (16), 11319−11327.
(44) Zhao, D.; Wang, Y.; Dong, C.-L.; Huang, Y.-C.; Chen, J.; Xue, F.; Shen, S.; Guo, L. Boron-doped nitrogen-deficient carbon nitride-

https://doi.org/10.1021/acsestengg.4c00949
ACS EST Engg. XXXX, XXX, XXX−XXX

based Z-scheme heterostructures for photocatalytic overall water splitting. *Nat. Energy* **2021**, *6* (4), 388−397.
(45) Liu, Q.; Cheng, H.; Chen, T.; Lo, T. W. B.; Xiang, Z.; Wang, F. Regulating the *OCCHO intermediate pathway towards highly selective photocatalytic CO_2 reduction to CH_3CHO over locally crystallized carbon nitride. *Energy Environ. Sci.* **2022**, *15* (1), 225−233.
(46) Zhao, D.; Dong, C.-L.; Wang, B.; Chen, C.; Huang, Y.-C.; Diao, Z.; Li, S.; Guo, L.; Shen, S. Synergy of Dopants and Defects in Graphitic Carbon Nitride with Exceptionally Modulated Band Structures for Efficient Photocatalytic Oxygen Evolution. *Adv. Mater.* **2019**, *31* (43), No. 1903545.
(47) Wenger, O. S. A bright future for photosensitizers. *Nat. Chem.* **2020**, *12* (4), 323−324.
(48) Zhang, Y.; Lee, T. S.; Favale, J. M.; Leary, D. C.; Petersen, J. L.; Scholes, G. D.; Castellano, F. N.; Milsmann, C. Delayed fluorescence from a zirconium(iv) photosensitizer with ligand-to-metal charge-transfer excited states. *Nat. Chem.* **2020**, *12* (4), 345−352.
(49) Hu, Y.; Zhong, Z.; Lu, M.; Muhammad, Y.; Jalil Shah, S.; He, H.; Gong, W.; Ren, Y.; Yu, X.; Zhao, Z.; Zhao, Z. Biomimetic O_2-carrying and highly in-situ H_2O_2 generation using Ti_3C_2 MXene/MIL-100(Fe) hybrid via Fe-Protoporphyrin bridging for photo-fenton synergistic degradation of thiacloprid. *Chem. Eng. J.* **2022**, *450*, No. 137964.
(50) Kong, J.; Xiang, Z.; Li, G.; An, T. Introduce oxygen vacancies into CeO_2 catalyst for enhanced coke resistance during photo-thermocatalytic oxidation of typical VOCs. *Appl. Catal., B* **2020**, *269*, No. 118755.
(51) Zhang, W.; Li, G.; Liu, H.; Chen, J.; Ma, S.; Wen, M.; Kong, J.; An, T. Photocatalytic degradation mechanism of gaseous styrene over Au/TiO_2@CNTs: Relevance of superficial state with deactivation mechanism. *Appl. Catal., B* **2020**, *272*, No. 118969.
(52) Zhang, J.; Vikrant, K.; Kim, K.-H.; Dong, F. Photocatalytic destruction of volatile aromatic compounds by platinized titanium dioxide in relation to the relative effect of the number of methyl groups on the benzene ring. *Sci. Total Environ.* **2022**, *822*, No. 153605.
(53) Zhang, Q.; Li, G.; Liu, W.; Li, G.; He, T.; Zhang, H.; Yu, Y.; Peng, H. Constructing highly active zeolite encapsulated PdAg alloy catalysts for typical VOCs deep oxidation: The role of electron-structure interaction. *Appl. Catal., B* **2024**, *352*, No. 124051.
(54) Li, J.; Dong, X.; Zhang, G.; Cui, W.; Cen, W.; Wu, Z.; Lee, S. C.; Dong, F. Probing ring-opening pathways for efficient photocatalytic toluene decomposition. *J. Mater. Chem. A* **2019**, *7* (7), 3366−3374.
(55) Mi, R.; Li, D.; Hu, Z.; Yang, R. T. Morphology Effects of CeO_2 Nanomaterials on the Catalytic Combustion of Toluene: A Combined Kinetics and Diffuse Reflectance Infrared Fourier Transform Spectroscopy Study. *ACS Catal.* **2021**, *11* (13), 7876−7889.

https://doi.org/10.1021/acsestengg.4c00949
ACS EST Engg. XXXX, XXX, XXX−XXX